Bulletin of the Seismological Society of America, 92, 1, pp. 161–171, February 2002

Deformation during the 12 November 1999 Düzce, Turkey, Earthquake, from GPS and InSAR Data

by Roland Bürgmann, M. Emin Ayhan, Eric J. Fielding, Tim J. Wright, Simon McClusky, Bahadir Aktug, Coskun Demir, Onur Lenk, and Ali Türkezer

Abstract Only 87 days after the M_w 7.5, 17 August 1999 İzmit earthquake, the Düzce earthquake ruptured a ca. 40-km-long adjoining strand of the North Anatolian fault (NAF) system to the east. We used displacements of 50 Global Positioning System (GPS) sites together with interferometric synthetic aperture radar (InSAR) range-change data spanning the event to estimate the geometry and slip distribution of the coseismic rupture. Postseismic deformation transients from the Düzce earthquake and the preceding İzmit event that are included in some of the measurements are corrected for using dislocation models fit to GPS data spanning the various time periods. Nonlinear inversions for fault geometry indicate that the rupture occurred on a ca. 54° north-dipping oblique normal, right-lateral fault. Distributed-slip inversions indicate maximum strike slip near the center of the Düzce fault close to the earthquake hypocenter. Slip magnitude and depth of faulting decrease to the west and east of the hypocenter. Both GPS and InSAR data suggest that normal slip is restricted to the shallow portion of the rupture. The Düzce earthquake had the highest slip-to-rupture-length ratio of any historic earthquake along the NAF.

Introduction

The likelihood of a significant earthquake to occur is increased near and soon after an earlier major event because of the changes in the associated stress field (Harris, 1998). The 12 November M_w 7.2 Düzce earthquake struck northwestern Turkey (Fig. 1), only 87 days after the adjoining 17 August 1999 İzmit earthquake (M_w 7.5). The Düzce earthquake is the latest in a classic sequence of $M \geq 6.7$ earthquakes that propagated ca. 1000 km along the North Anatolian fault (NAF) since the $M_w \approx 7.9$, 1939 Erzincan earthquake in eastern Turkey (Toksöz *et al.,* 1979; Barka, 1996; Stein *et al.,* 1997). The occurrence of sequential earthquakes along the NAF in general, and the İzmit–Düzce sequence in particular, have been interpreted in terms of static Coulomb stress transfer, advancing subsequent events on the adjacent fault segments (Toksöz *et al.,* 1979; Stein *et al.,* 1997; Hubert-Ferrari *et al.,* 2000; Parsons *et al.,* 2000). In addition to static coseismic stress changes, postseismic deformation transients from the İzmit event might have played a role in the loading and triggering of the Düzce event (Reilinger *et al.* 2000; Hearn *et al.,* 2002).

In this study, we use all the available Global Positioning System (GPS) and interferometric synthetic aperture radar (InSAR) measurements of surface displacements during the Düzce earthquake to constrain the geometry and slip distribution of the rupture. This kinematic information is essential for models of fault interaction to better understand the role of the preceding İzmit earthquake in the timing, location, kinematics, and slip distribution of the Düzce earthquake (Hubert-Ferrari *et al.,* 2000; Parsons *et al.,* 2000; Hearn *et al.,* 2002), and for computations of stress changes in the region resulting from this latest large earthquake along the NAF zone.

Setting and Other Observations of the Düzce Earthquake

The Düzce earthquake occurred along a branch of the NAF system in northwestern Turkey. The western NAF accommodates ca. 25 mm/yr of Anatolia–Eurasia right-lateral motion (Straub *et al.,* 1997; McClusky *et al.,* 2000). Whereas deformation is dominantly accommodated along a single fault strand east of ca. 32° E, the NAF splays into two active branches in northwestern Turkey. Near Bolu, the NAF branches into a southern strand, which ruptured during the $M \approx 7$ 1957 Abant and 1967 Mudurnu Valley earthquakes (Barka, 1996) and the Düzce and Karadere fault segments to the north, bounding the uplifted Almacik block in between (Sengör *et al.,* 1985). The northern strand has not ruptured during the twentieth century (Barka, 1996). Analysis of repeated GPS data suggest that up to 10 mm/yr of NAF slip are accommodated on the Düzce–Karadere fault strand (Ayhan *et al.,* 1999). The İzmit earthquake rupture included the

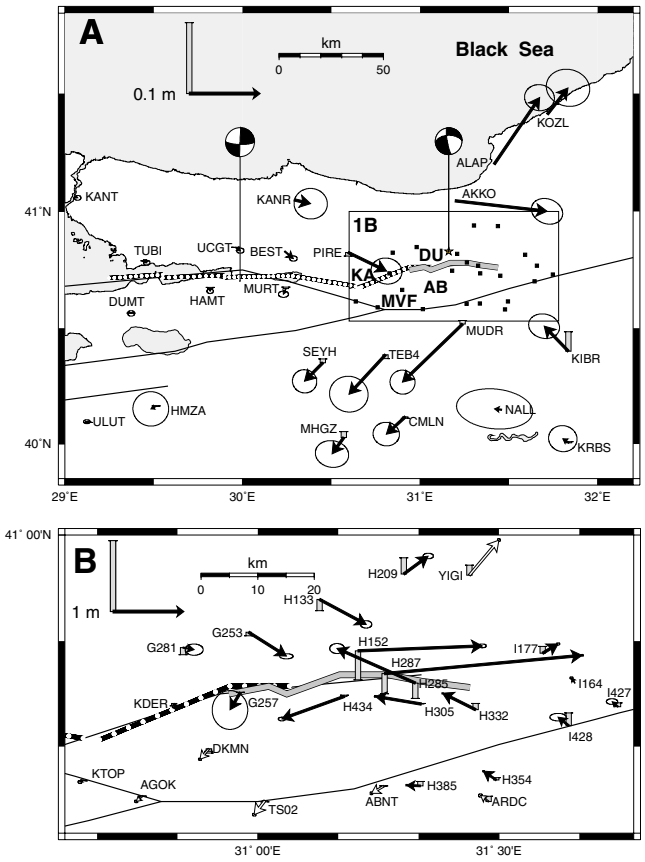

Figure 1. Fault map with GPS-measured Düzce earthquake surface displacements corrected for deformation before and after the event. Arrows tipped with 95% confidence ellipses are horizontal motions and flat-tipped gray-shaded bars indicate the vertical displacements. Uncertainties (one standard deviation) of vertical displacement estimates range from 5 to 105 mm and are not shown for clarity. (A) Regional view showing the focal mechanisms (Harvard catalog centroid moment tensor) of the 17 August 1999 Izmit and 12 November 1999 Düzce earthquakes. KF, Karadere fault segment; DF, Düzce fault; MF, Mudurnu fault segment; AB, Almacik block. Dotted line follows the Izmit earthquake rupture, the gray shaded line indicates the Düzce rupture surface trace. Boxed area is shown in close up in (B). Open arrows in (B) are from Ayhan *et al.* (2001). Note difference in the displacement scale in (A) and (B).

Karadere and westernmost Düzce segments (Fig. 1), and the Düzce earthquake ruptured most of the Düzce fault segment.

The Düzce and Karadere fault segments accommodate relative uplift of the Almacik block over a basin and topographical depression to the north, and have been interpreted as steeply south-dipping reverse faults (Sengör *et al.,* 1985). Focal mechanism determinations for the Düzce earthquake reveal a steeply (55°–66°) north-dipping nodal plane with a small component of normal slip, in addition to a dominant right-lateral component (Table 2, Fig. 1). Available hypocentral depth estimates range from 10 to 18 km (Table 2). Geologic investigations of the ca. 40-km-long surface rupture reveal up to 4.9 m right-lateral offsets, with subsidiary north-side-down vertical offsets along the western ca. 15 km of the rupture. The westernmost Düzce fault rupture also broke with minor (≤20 cm) offsets in the preceding İzmit event.

Coseismic Surface Displacements from GPS and InSAR Measurements

GPS Measurements

Because the Marmara Sea region had been identified as a seismic gap likely to generate significant earthquakes (Toksöz *et al.,* 1979), a substantial GPS monitoring effort was underway prior to the İzmit–Düzce earthquake sequence to measure the strain accumulation along the NAF (Straub *et al.,* 1997; McClusky *et al.,* 2000). The Marmara Sea region monitoring effort includes installations of continuously recording stations, which help us to separate immediate coseismic displacements from early postseismic deformation. In response to the occurrence of the 17 August 1999 İzmit earthquake, repeated GPS measurements were made throughout the region just prior to the Düzce earthquake (Ergintav *et al.,* 2002). Furthermore, the General Command of Mapping (GCM) conducted regional and local surveys to repeat GPS measurements and to establish additional geodetic control points.

In this study, we integrate data from 33 stations previously described by Ayhan *et al.* (2001) with measurements of 17 additional stations in the epicentral region, which were surveyed in short (∼45 min) occupations between 27 September and 8 October 1999 and ca. 8-hr occupations on 14–15 April 2000 by the GCM surveying group. The new GPS data were processed at GCM using the GAMIT/GLOBK GPS processing software in a consistent manner with the solutions of Ayhan *et al.* (2001), following procedures described by McClusky *et al.* (2000). Because of the short occupation times, the uncertainties of displacements from these new data are significantly larger than those computed from the commonly used 8- to 24-hr solutions (Fig. 1b).

For continuously operating stations, we differenced coordinates from 2 days before and 2 days after the event and applied no further corrections. Measurements of stations occupied within 7 days of the earthquake are also differenced without corrections. However, the motions of most GPS sites are corrected for postseismic transient deformation from both the İzmit and Düzce earthquakes to avoid contamination of the coseismic displacement estimates. Corrections of the original data set are described by Ayhan *et al.* (2001).

The October 1999 to April 2000 measurements of the near-fault sites need to be corrected for transient deformation from both the İzmit and Düzce earthquakes, as well as the background secular strain. The background strain field is well constrained by 1988–1997 GPS velocities in the area (McClusky *et al.,* 2000), which are well fit by a single-fault

model (Table 1). The geometry and slip rate of the secular dislocation model are inverted from the velocities of 45 GPS sites, located between 28° E and 33° E and between 38.5° N and 42° N. This model is used solely to compute good estimates of secular velocities and is not a realistic model of the strain accumulation process in the region (Meade *et al.,* 2002). A single dislocation is fit to the GPS data collected during the 40 days before the earthquake, which are affected by post-İzmit earthquake relaxation. Lastly, we use a preliminary afterslip model inverted from the GPS data spanning the first 110 days following the Düzce earthquake, to correct for deformation during this period caused by relaxation processes from both events (Table 1). The largest correction vector for transient deformation amounts to 47 mm at station G253 (Fig. 1b), which is 7% of the measured motion. Although corrections are rather insignificant for the near-field sites with large coseismic offsets, they are more important at larger distance. Figure 1 shows the corrected coseismic station displacements and their 95% confidence ellipses.

The combined GPS network is well distributed about the Düzce earthquake rupture, with sites spaced about 10 km apart in the epicentral region (Fig. 1). Significant motions were measured at distances of up to ca. 100 km from the epicenter. The pattern of displacements is consistent with a dominantly right-lateral rupture; the vertical displacements, however, suggest an additional component of north-side-down, south-side-up motions. Sites to the north of the rupture displaced somewhat more than sites at similar distance to the south, which suggests that the rupture is northward dipping.

InSAR Measurements

Space-based InSAR can map ground deformation at tens of meters spatial resolution with centimeter precision (Massonnet and Feigl, 1998; Bürgmann *et al.,* 2000); however, a single InSAR image only provides measurements of one component of the displacement field along the look direction of the radar. In addition, errors caused by tropospheric signal delays and orbit-parameter uncertainties can be substantial. Thus, to improve our model resolution, we compare and integrate the GPS measurements of three-dimensional site displacements with InSAR measured range changes between the two SAR images from the European Space Agency's (ESA) Earth remote sensing (ERS) spacecraft collected on 14 September 1999 and 22 November 1999 (Fig. 2). The SAR images of frames 794 and 812 along the ERS-spacecraft ascending-orbit track 114, were taken by the ERS-2 spacecraft (orbit 23014 on 14 September 1999) and by the ERS-1 spacecraft (orbit 43689 on 22 November 1999), respectively. Unfortunately, there are no suitable data (sufficiently short temporal and orbit baselines) from the descending orbit (track 21), which would have provided range-change data along a different look direction.

The raw data are processed using the InSAR processing software developed at the Jet Propulsion Laboratory (Rosen *et al.,* 1996). Topographic contributions to the apparent range changes are removed using a ca. 90-m posting digital elevation model (DEM) (Fig. 2a). The orbital baseline separation of the two ERS-spacecraft passes results in a 2π change in phase (28-mm range change) for every 165 m of uncorrected elevation differences; the so-called ambiguity height (Bürgmann *et al.,* 2000). Densely vegetated areas and rough topography limit the region of adequate correlation, in particular, in the agricultural area north of the surface rupture and the steep terrain of the Almacik block to the south (Fig. 2b).

The data are processed at 2 by 10 looks (averaging 20 pixels to produce a pixel ground size of ca. 40 m), because the range-change gradient just to the north of the rupture is so high that the phase change across a larger pixel size exceeds π and thus would lead to complete decorrelation in the zone of largest deformation. The interferogram is filtered using a weighted power spectrum technique (Goldstein and Werner, 1998) to produce the wrapped interferogram shown in Figure 2b. The contribution of phase caused by the orbital separation of the two ERS images was calculated from the

Table 1

Fault Parameters for Corrections of Earthquake Displacement Measurements Derived from Inversions of Pre- and Post-Düzce Earthquake GPS Data*

Model (mm/dd/yy)	Length (km)	Depth (km)	Width (km)	Dip (°N)	Strike (°)	Latitude (°)	Longitude (°)	Dip Slip (m)	Strike Slip (m)
Secular correction:									
1988–1997 (m/yr)	1526	24.4	3000	90	86.4	40.77	31.5	–	0.033 m/yr
GPS correction:	82.7	28.1	15.4	90	90.4	40.72	30.16	–	0.19
10/01/99–11/12/99	28.4		17.2	51.3	88.1	40.76	31.25	0.76	3.75
11/13/99–04/20/00									
	35		15	90		40.73	30.02	0.21	0
	25.2		6	60.0		40.74	30.84	0.09	0.04
	45.2		5	65.3		40.78	31.33	0.15	0
InSAR correction:									
09/14/99–11/12/99	82.4	28.1	15.4	90	90.3	40.72	30.16		0.29
11/13/99–11/22/00	119	32.1	17.5	90.7	88.2	40.84	30.94	0.01	0.12

*Latitude and longitude refer to the center of surface fault trace.

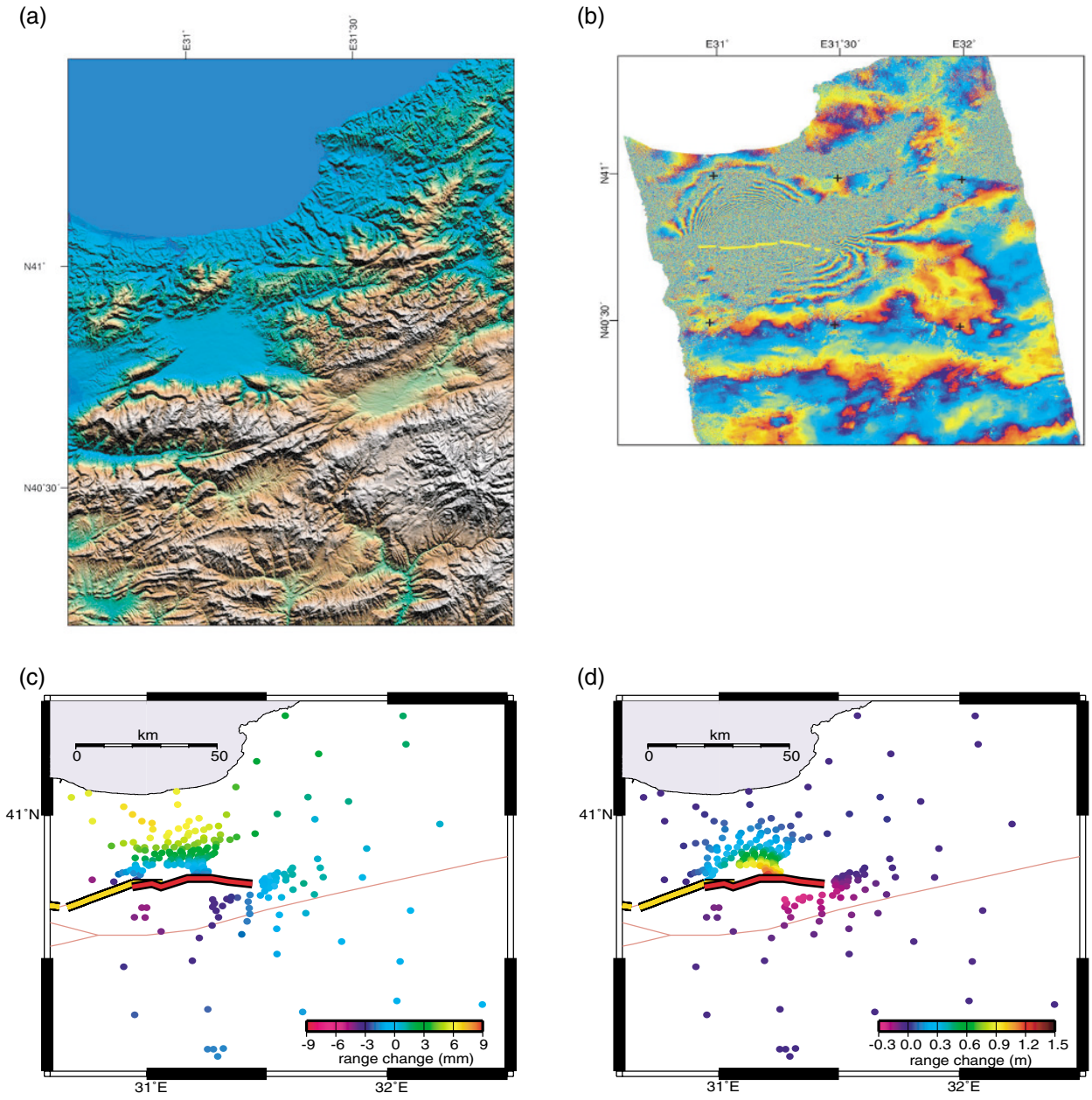

Figure 2. (A) Shaded relief map of the epicentral region. The Düzce fault separates the uplifted Almacik block to the south and a topographic depression and sedimentary basin to the North. (B) Interferogram computed from the 14 September and 22 November 1999 ERS SAR images at ca. 40-m pixel spacing. Each fringe or color cycle indicates a 2π-phase cycle corresponding to a 28-mm relative range change. The coherence is best (clear fringes) in developed areas and dryer highlands to the north and south. Coherence is insufficient for construction of an interferogram in the agricultural region to the north of the rupture and in the rough topography of the Almacik block to the south. (C) Correction applied to the InSAR range-change data to account for 2 months of pre-earthquake deformation and 10 days of postDüzce earthquake deformation contained in the interferogram. The corrections are computed from dislocation models representing secular strain accumulation and postseismic afterslip inverted from GPS measurements (Table 1). Color scale in millimeter. (D) Manually unwrapped and subsampled range-change data digitized from wrapped interferogram and corrected for deformation that occurred before and after the Düzce earthquake. The line-of-sight range changes are shown as colored circles. The color bar indicates the scale of relative range change in meters.

precise (PRC) orbits of the ESA German Processing and Archiving Facility (D-PAF). The interferogram is geocoded to a Universal Transverse Mercator projection using the DEM. Surface displacements are computed from the interferogram by digitizing the 2π phase fringes and converting the phase delay into relative line-of-sight range changes between the two scenes (Wright *et al.,* 1999) to produce 234 line-of-sight range-change measurements. Only every second fringe is included in the high gradient region to the north of the rupture.

The 14 September to 22 November InSAR range-change measurements also include transient deformation following the İzmit and Düzce earthquakes. We thus use afterslip models inverted from GPS measurements collected during a 60-day period before and a 10-day duration after the Düzce earthquake to compute range-change corrections at each image point (Table 1). The maximum correction amounted to 6.6 mm to the north of the epicentral region (Fig. 2c).

The final corrected data set for the model inversions for coseismic rupture parameters is shown in Figure 2d. The coseismic range-change pattern is asymmetric about the Düzce rupture with up to 1.2 m of range increase measured to the north and up to 0.25 m of range decrease measured to the south. Range increase north of the rupture is consistent with subsidence and/or horizontal motion away from the eastward-looking ERS spacecraft, as would be caused by right-lateral faulting or dip-slip faulting.

The ERS ascending orbit track trends N12° E with the radar looking eastward at a look angle varying from 18° to 28° off-vertical. Surface displacements and resulting range change are related as $\Delta\rho = \mathbf{\Delta d} \cdot \mathbf{e}$, where $\Delta\rho$ and $\mathbf{\Delta d}$ are the range change and surface displacement vector, respectively, and $\mathbf{e}$ is the unit vector in the range direction. As the look angle varies across the image, we compute $\mathbf{e}$ individually for each image point used in the model inversions.

Rupture Geometry and Slip Distribution

The displacements of the points at the Earth's surface caused by the Düzce earthquake reveal information about the rupture geometry and the distribution of fault slip. We model the observed coseismic displacements and range changes using rectangular dislocations in an elastic, homogeneous, and isotropic half-space (Okada, 1985). We choose a Poisson's ratio of 0.25, which is equivalent to specifying that the two Lamé parameters μ and λ in Hooke's law are equal (Okada, 1985). Our inversions attempt to minimize the weighted residual sum of squares $WRSS = (\mathbf{d}_{obs} - \mathbf{d}_{mod})^T \times \mathbf{cov}^{-1} \times (\mathbf{d}_{obs} - \mathbf{d}_{mod})$, where $\mathbf{d}_{obs}$ and $\mathbf{d}_{mod}$ are the observed and modeled motions, respectively, and $\mathbf{cov}$ is the diagonal data covariance matrix. The GPS errors of the horizontal and vertical displacements are derived from the formal GPS-analysis uncertainties. The subsampled InSAR data are modeled as uncorrelated with 10-mm standard deviations. In addition to solving for the model fault parameters, we also estimate a constant offset and two orbital tilt parameters (a linear slope across the interferogram) when including InSAR data. In the geometry inversions, we attempt to find the optimal location and orientation of the model fault plane. In the slip-distributed models discussed subsequently, we increase the size of the optimal fault plane and subdivide it into a grid of smaller fault elements and determine the optimal slip vector on each patch. We commonly apply additional constraints to the inversions, such as holding certain geometry parameters fixed or applying smoothing or nonnegativity constraints to the slip-distributed models. Furthermore, we consider surface offsets across the rupture determined from field measurements for comparison with slip-distributed models.

Geometry Inversions of GPS and InSAR Data

For the geometry inversions, we use a constrained, nonlinear optimization algorithm (Arnadottir and Segall, 1994; Bürgmann *et al.,* 1997), which allows us to estimate the geometry (parameterized by length, depth, width, dip, strike, and location) and the strike-slip and dip-slip offsets of one or more faults that best fit the GPS data. The only constraint imposed on the geometry inversion is that the fault must reach the surface; that is, the depth to the upper dislocation edge is set to zero while we solve for the remaining parameters. To ensure that we find the global minimum in the nonlinear inversion scheme, we use a number of different starting models. As long as the starting model is placed in close vicinity of the surface rupture, the inversion finds the same optimal model with each starting model.

We compare rupture geometry inferred from the separate GPS and InSAR data sets and the joint inversions. We find that the optimal uniform-slip dislocations determined in all the inversions roughly follow the surface rupture mapped in the field and are consistent with each other and with the independent seismologic evidence (Table 2, Fig. 3a). The GPS data support a somewhat steeper dip angle (60°) than that inferred from the InSAR data (52°). We note that Ayhan *et al.* (2001), using the previously available subset of the GPS data that did not include many sites close to the rupture (Fig. 1b), found a 51°-dip angle. The joint inversion of the GPS and InSAR data results in a model with most parameters lying in between those found from the separate inversions. The joint inversion results in increased misfits to both data sets by about 60% and 25%, for the GPS and InSAR data, respectively.

The optimal model fault determined from the joint inversion of the GPS and InSAR data strikes N85° E, dips 57° to the north on a 21.5-km-long and 16-km-wide rupture to a depth of 13 km, and slipped 4.9 m right-lateral and 0.5 m north-side down (Table 2). The geodetic moment magnitude of this Düzce earthquake model is M_w 7.14, assuming a shear modulus of 30 GPa. Figure 3a shows the residual (observed minus modeled motions of GPS sites and InSAR range changes) displacements of the single-fault model. This simple model provides a good fit to the geodetic measure-

Table 2
Fault Parameters from Inversions of GPS and/or InSAR Data and Seismic Studies*

Model	Length (km)	Width (km)	Dip (°N)	Strike (°)	Latitude (°)	Longitude (°)	Dip Slip (m)	± (1-σ)	Strike Slip (m)	± (1-σ)	WRSS	Misfit	M_0 N m	M_w
Single-fault (GPS)	24.95	15.74	60.17	85.28	40.78	31.25	0.37	0.02	4.29	0.02	617	4.26	5.08×10^{19}	7.14
Single-fault (InSAR)	20.65	16.16	52.06	79.67	40.75	31.28	0.22	0.01	5.76	0.02	2999	13.10	5.77×10^{19}	7.17
Single-fault	21.45	16.21	56.65	84.50	40.76	31.26	0.50	0.01	4.90	0.02	1015	7.00	5.14×10^{19}	7.14
(GPS and InSAR)											3765	16.44		
Double-fault model	7.70	14.99	63.17	85.67	40.75	31.14	2.25	0.03	3.95	0.04	823	5.76	5.22×10^{19}	7.15
(GPS and InSAR)											1236	5.44		
	18.83	14.21	51.11	83.66	40.76	31.30	0.16	0.01	4.54	0.02				
Distributed slip (GPS)	48.65	24.5	54	86.67	40.77	31.20					194		5.51×10^{19}	7.16
Distributed slip (InSAR)	48.65	24.5	54	86.67	40.77	31.20					169		5.62×10^{19}	7.17
Distributed slip	48.65	24.5	54	86.67	40.77	31.20					321		5.66×10^{19}	7.17
(GPS + InSAR)											224			
Seismic studies		Depth												
USGS NEIC		14	59	96	40.77	31.15							4.5×10^{19}	7.1
Harvard CMT		18	54	88	40.93	31.25							6.65×10^{19}	7.2
Yagi and Kikuchi (1999)		10	65	85	40.8	31.2							5.6×10^{19}	7.1

*Latitude and longitude refer to the center of surface fault trace or the moment tensor centroid.

ments at larger distances. However, displacements near the rupture are not very well matched. We also note that the model dislocation is significantly shorter than the observed surface rupture and is located along the eastern rupture segment. Our measure of misfit, which accounts for the number of model parameters P and number of data N, $\sqrt{\mathrm{WRSS}/(N-P)}$, is much greater than 1 for either data set, suggesting that the data can resolve additional details about the rupture. Whereas the İzmit earthquake was dominantly a strike-slip event on a vertical fault (Reilinger *et al.,* 2000), the Düzce earthquake had a significant normal faulting component on a steeply north-dipping fault plane.

If we allow for a second dislocation in the geometry inversion, the rupture is separated into two adjoining segments, where the eastern segment is favored to have dominantly strike slip on a 51°-dipping fault plane (Table 2). The 8-km-long western segment is favored to have greater than 2 m of dip slip, in addition to 4 m strike slip. The surface projections of the two model dislocations are shown in Figure 3b as black rectangles, together with the data residuals.

Slip-Distributed Models

We evaluate more detailed rupture models to resolve additional information about the subsurface coseismic slip distribution with the two geodetic data sets and surface slip measurements. The mapped coseismic surface rupture and best-fit single-fault model define the geometry of the model fault. Our best-fitting single-fault model from the joint GPS–InSAR inversion is enlarged at the down-dip and lateral edges for a 49- by 24.5-km fault plane, which is further discretized into 3.5-km-long, 3.5-km-wide patches (14 by 7 elements) for the distributed slip inversions. We invert for the optimal slip distribution and seek models that minimize the misfit, while preserving smoothness of the model slip distribution. Smoothing and nonnegativity (right-lateral and normal slip only) constraints are applied to avoid models with unreasonable (oscillating) slip patterns that are favored by a free inversion without such additional constraints (Harris and Segall, 1987; Du *et al.,* 1992). A finite-difference approximation of the Laplacian imposes smoothness constraints on the slip distribution (Harris and Segall, 1987). We do not apply any edge constraints; that is, slip at the bottom and lateral ends of the model rupture are not minimized.

In the single-fault geometry inversions, we found different rupture dips for the GPS and InSAR inversions, and inversions of the GPS data set reported by Ayhan *et al.* (2001). The optimal dip angle of slip-distributed models can not be assumed to be the same as that found in the geometry inversion for a uniform-slip dislocation. Thus, while constraining the remaining geometry parameters, we evaluate the misfit of the slip-distributed models for northward dips varying from 30° to 90°. Figure 4 illustrates the optimal dip angles (minimizing the WRSS) for the inversion of the individual GPS (54°) and InSAR (59°) data sets and for the joint inversion. The data clearly rule out the near-vertical dips of most strike-slip faults in the region. The final best-fitting dip based on the joint inversion is 54° and is used for all the models discussed subsequently.

In smoothed, distributed slip models there is a trade-off between the misfit and smoothness of the model slip distribution. We follow previous studies (Harris and Segall, 1987; Du *et al.,* 1992) in determining the penalty factor β, which determines the relative weight of the smoothness constraint. Figure 5 shows the *WRSS* as a function of the model roughness $|G_{\mathrm{lap}}\mathbf{S}|^2$, where G_{lap} is the finite-difference approximation of the Laplacian operator and $\mathbf{S}$ is the vector of fault slips. Increasing β leads to a reduction in roughness at the cost of increasing misfit. We choose a value of β equal to 0.7 beyond which increasing model roughness is not re-

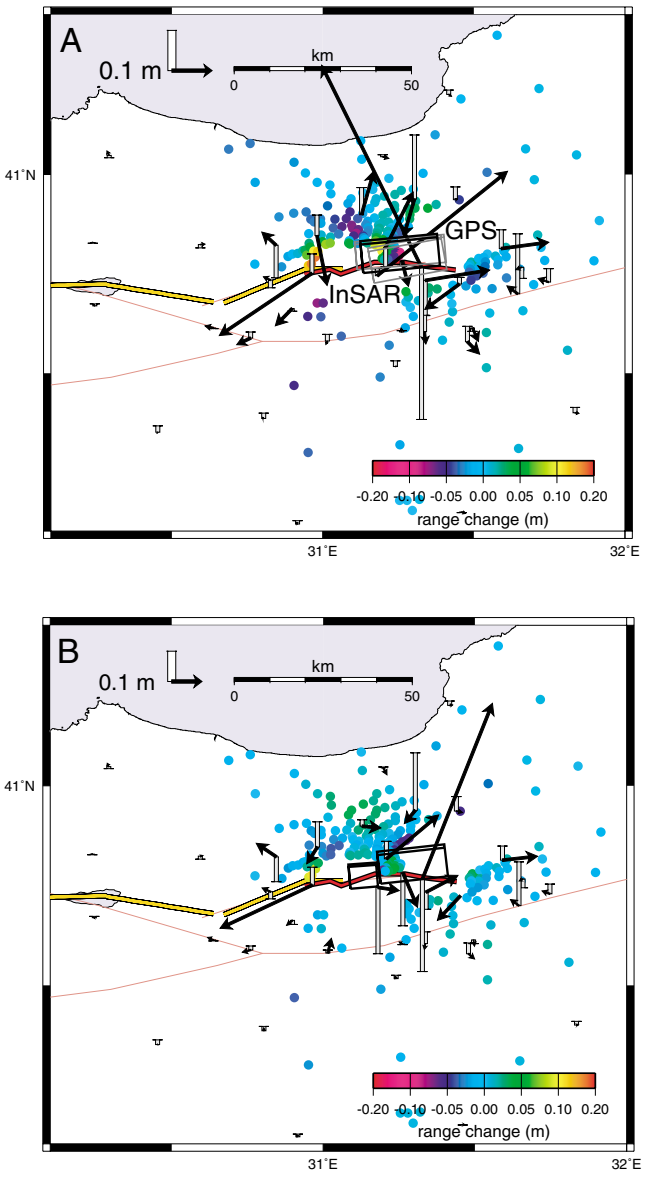

Figure 3. (A) Comparison of single-fault geometry inverted from GPS and InSAR deformation measurements and residuals from joint inversion of GPS and InSAR data. Bold black rectangle is surface projection of best-fit dislocation from the joint inversion. The labeled gray rectangles are best-fit single-fault models from separate inversions of the GPS and InSAR data (Table 3). Also shown are residual (observed minus predicted), horizontal (arrows), and vertical (N–S-trending flat-tipped bars) station displacements from the joint inversion of the two data sets. Only residuals from within ca. 100 km of the rupture are shown. Colored circles are the range-change residuals of the InSAR data from the joint inversion (color bar indicates scale in meters). (B) Same as in (A) for best-fitting two-fault model inverted from combined GPS–InSAR data set.

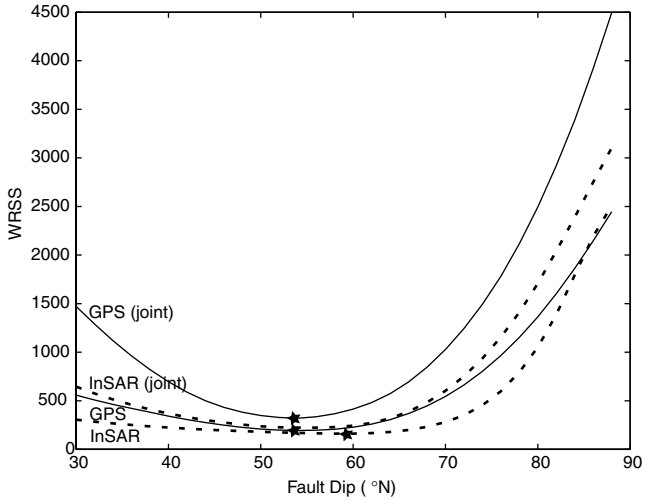

Figure 4. Plot of WRSS versus northward dip of rupture plane for distributed-slip models inverted from GPS (solid lines) and InSAR (dashed lines) data and from joint inversions. All other fault geometry parameters are fixed. Labels indicate the respective data sets used in the inversions. Stars indicate best-fit dips for individual and joint inversions. For the joint inversion, the WRSS of the GPS and InSAR data are shown separately. The final best-fitting dip based on the joint inversion is 54°.

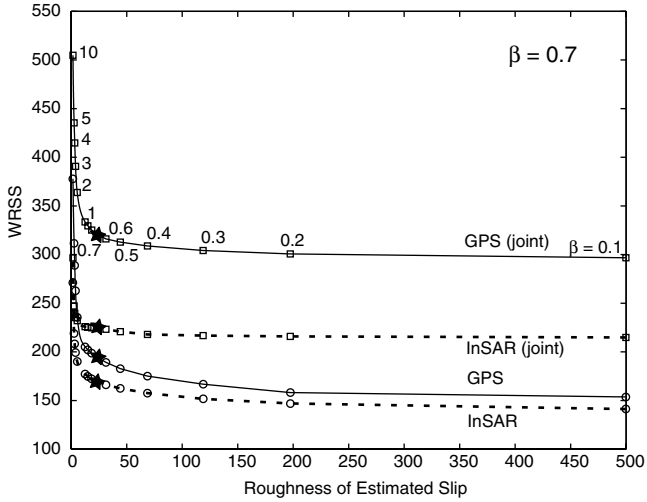

Figure 5. Plot of WRSS as a function of the roughness of the estimated slip distributions for a range of smoothing factors for both individual inversions of the GPS (solid lines) and InSAR (dashed lines) data sets and joint inversions. Selected points are labeled with the respective penalty factor β. Stars indicate the smoothing factor ($\beta = 0.7$) used in the inversions shown in Figures 4 and 6.

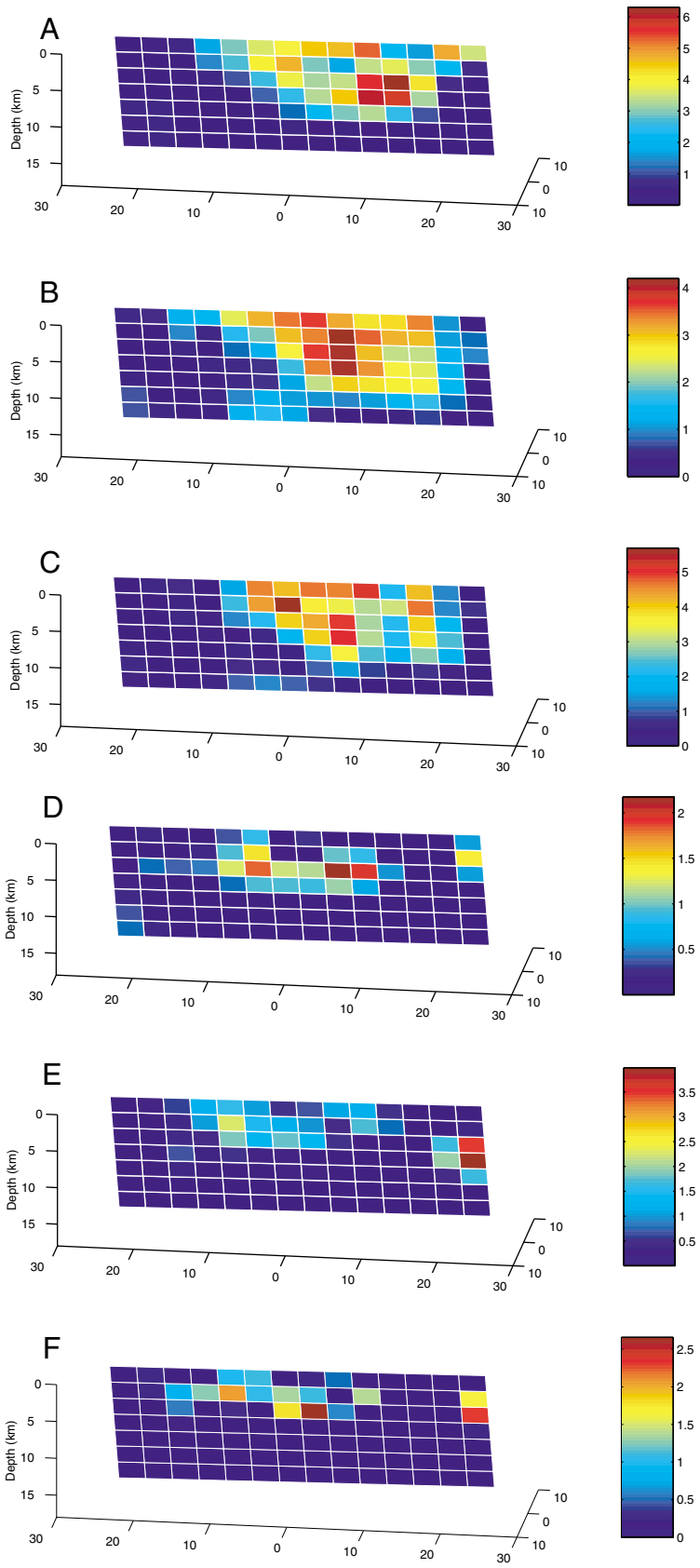

Figure 6. Distributed slip models. (A) Strike-slip distribution on Düzce rupture from GPS data in perspective view from the south. (B) Strike-slip distribution from InSAR data. (C) Strike-slip distribution from joint inversion of GPS and InSAR data. (D) Normal-slip distribution from GPS data. (E) Normal-slip distribution from InSAR data. (F) Normal-slip distribution from joint inversion of GPS and InSAR data.

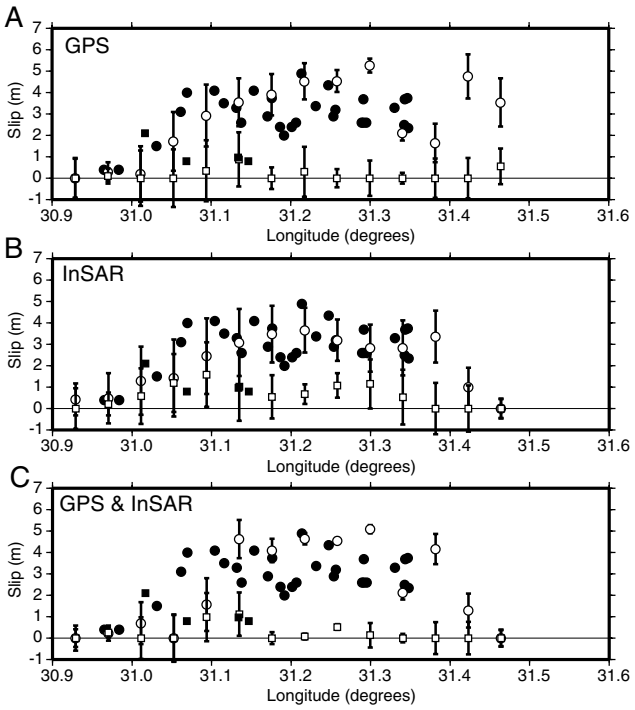

Figure 7. Comparison of surface offsets from field measurements (Ayhan *et al.,* 2001) and model offsets from inversion of the (A) GPS, (B) InSAR, and (C) joint data sets on top row of slip patches. Mapped strike-slip and dip-slip offsets are solid circles and squares, respectively. Measurement uncertainties are estimated at ca. 0.2 m. Modeled strike slip and dip slip are shown as open circles and squares together with their 1-sigma uncertainties.

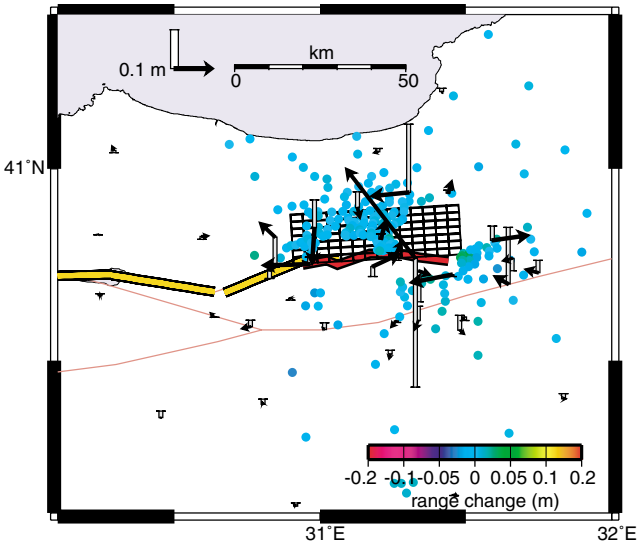

Figure 8. Residuals (observed minus predicted) from joint distributed-slip inversion of GPS and InSAR data. GPS residuals include horizontal (arrows) and vertical (N–S-trending flat-tipped bars) station displacements. Colored circles are the range-change residuals of the InSAR data from the joint inversion (color bar indicates scale in meters). Black rectangles are surface projection of the dislocation grid.

warded with substantially better misfits in either individual or joint inversions.

Figure 6a–c shows the strike-slip distributions inverted from the GPS data, the InSAR data, and the joint data set, respectively. Figure 6d–f shows the respective normal-slip distributions. All models use a penalty factor of β equal to 0.7 and have a northward dip of 54°. Although the overall patterns are similar, important differences remain between the GPS- and InSAR-derived slip distributions. Both data sets suggest similar maximum slip magnitudes and very similar geodetic moments (Table 2). Coseismic slip deepens gradually from west to east toward a maximum, just east of the center of the model rupture. The maximum strike slip appears westward shifted in the InSAR-derived pattern and is of lower magnitude compared with the GPS inversion. Both data sets suggest that dip slip is relatively shallow and distributed among several patches that do not correlate well with the strike-slip distribution.

The surface slip distribution determined in our models can be compared to geologic surface slip measurements. Figure 7 shows the observed surface slip distributions (Ayhan *et al.,* 2001), together with those predicted along the top row of the models shown in Figure 6. We find that all the models match the observed offsets along the central rupture, but underestimate strike slip somewhat west of the rupture center. Furthermore, the GPS data suggest a rupture that extends further east than indicated by the mapped surface breakage. Figure 8 shows the remaining residuals of the distributed slip models. Some of the sites right along the coseismic rupture remain badly matched by the data.

Discussion and Conclusions

The geodetic data clearly rule out a near-vertical geometry of the Düzce earthquake rupture (Fig. 4). Geodetic constraints are consistent with seismologic studies and provide additional details of the kinematics of the earthquake. The geodetic coseismic moment estimates of M_0 = 5.1–5.7 $\times$ 10^{19} N m (M_w = 7.14–7.17) are within the range of seismic moments reported for the mainshock (M_0 = 4.5–6.6 $\times$ 10^{19} N m). Inversions of teleseismic data for focal mechanisms suggest a 54°–65° north-dipping nodal plane, consistent with the geodetic inversions. The north-dipping geometry is also supported by the observation that the aftershocks predominantly occur to the north, in the hanging-wall block of this oblique-normal rupture. A northward-down normal faulting component is also unambiguously supported by the geodetic data. Thus, the Almacik block is bounded in the north by a steeply north-dipping normal fault, rather than by south-dipping reverse faults, as postulated by Sengör *et al.* (1985). The oblique-normal faulting kinematics

of the Düzce fault is somewhat surprising, as this fault continues along the same, plate-motion parallel strike as the pure strike-slip rupture of the İzmit earthquake to the west. Further study is required to better understand the kinematics of the Düzce fault in the context of the complex branching geometry of the NAF zone in this area.

Teleseismic-waveform inversions reported by Yagi and Kikuchi (1999) indicate that the Düzce earthquake nucleated near the bottom center of the northward-dipping rupture and propagated bilaterally east and west, producing a relatively simple slip distribution. The slip-distributed models inverted from geodetic data are consistent with this relatively simple pattern, with a single broad strike-slip maximum about the earthquake hypocenter. Both geodetic data sets suggest that dip slip is restricted to the upper 10 km of the rupture.

The homogeneous, elastic half-space model does not allow for changing rigidity with depth, which together with other simplifying assumptions (no topography, no lateral variations of constitutive properties, purely elastic behavior), can lead to bias in the inversions (Okada, 1985; Savage, 1998). Finite-element modeling of the 17 August İzmit earthquake shows that models with higher rigidities in the lower crust and upper mantle require somewhat higher slip values at depth than suggested by the homogeneous half-space model (Hearn *et al.,* 2002).

Overall, the GPS and InSAR data suggest consistent rupture characteristics, but obvious differences remain. Such differences might be caused in part by unrecognized errors in either data set. In particular, atmospheric artifacts in the InSAR data are difficult to separate from range change caused by deformation, unless we have more redundant interferograms spanning the event. Additional differences could be explained by the different spatial distribution of the observations and remaining errors in the corrections for deformation not due to the earthquake. The near-surface offsets inferred from both GPS and InSAR data compare well to those observed in field measurements. Some significant discrepancies are likely because of the lack of GPS sites and coherent InSAR data very close to the rupture that limits our resolution of near-surface slip, especially along the western third of the rupture. Missing details of the rupture geometry in the model parameterization, likely effects of inelastic deformation, and heterogeneous rheology of the upper few kilometers of the crust might also cause such discrepancies.

We estimate a linear tilt across the range-change data as two free parameters in the model inversion, which accounts for error in the precise-orbit information of the ERS spacecraft. Using precise orbits, a residual linear gradient across an interferogram can be as large as ca. 2–3 fringes (56–84 mm) per 100 km in the range direction, and ca. 0.5–1 fringes (14–28 mm) per 100 km in the azimuth direction (Scharoo and Visser, 1998; Wright *et al.,* 2001). In the distributed slip inversion of the InSAR data alone, we estimate a gradient of 39 ± 6 mm per 100 km in the range direction and a gradient of -1 ± 5 mm per 100 km in the azimuth direction. In the joint inversion with the GPS data, the inversion finds tilts of 44 ± 4 mm per 100 km and -1 ± 4 mm per 100 km in the range and azimuth directions, respectively. The tilt parameters are within the range expected from the precision of the orbit information. The agreement of the corrections estimated with and without the constraints provided by the GPS data, suggests that in this case the inversion is able to determine a linear phase gradient caused by orbit errors from the InSAR data alone. This is aided by the inclusion of data well south of the zone of significant deformation.

The history of sequential earthquakes along the NAF suggests that fault interaction and earthquake triggering play an important role in the timing and location of major earthquakes (Stein *et al.,* 1997; Hubert-Ferrari *et al.,* 2000; Parsons *et al.,* 2000). Hearn *et al.* (2002) found that in addition to the coseismic stress changes during the İzmit earthquake, the rapid postseismic deformation that followed the event contributed substantially to the Coulomb stress changes on the eventual rupture at the hypocenter of the Düzce earthquake. In addition to promoting or inhibiting events on nearby faults, stress changes might also impact the size and slip distribution of subsequent events (Hudnut *et al.,* 1989; Perfettini *et al.,* 1999; Parsons and Dreger, 2000). Ayhan *et al.* (2001) found that the ratio of fault slip to rupture length along the Düzce fault was higher than in any previous historic earthquake along the NAF (Wells and Coppersmith, 1994). In part, this can be attributed to subsurface slip extending eastward past the ruptured surface trace and the north-dipping fault geometry, which enhances the slip-to-rupture-length ratio, as it allows for a larger rupture area for a given rupture length. More importantly, the Düzce earthquake was effectively part of a composite rupture with the preceding İzmit event and has a slip magnitude more consistent with the combined rupture length of about 160 km.

Acknowledgments

This research was supported in part by NSF grants to MIT EAR-9909730 and INT-9909619. We thank TUBITAK MRC for providing GPS data from continuous stations of the Marmara GPS network supported by World Bank Grant Number: 3511-TU. A NERC research studentship, with Nigel Press Associates, supported T.J.W. and ERS data were acquired under an ESA A03-213 grant to Oxford. This work also benefited from the discussions with Barry Parsons, Elizabeth Hearn, Semih Ergintav, and Rob Reilinger. Part of this research was performed at the Jet Propulsion Laboratory, California Institute of Technology, under a contract with the National Aeronautics and Space Administration. R.B. thanks his colleagues at MIT for their hospitality during a sabbatical semester at the Department of Earth, Atmospheric, and Planetary Sciences. This is Berkeley Seismological Laboratory Contribution No. 02-02.

References

Arnadottir, T., and P. Segall (1994). The 1989 Loma Prieta earthquake imaged from inversion of geodetic data, *J. Geophys. Res.* **99,** 21,835–21,855.

Ayhan, M. E., R. Bürgmann, S. McClusky, *et al.* (2001). Kinematics of the $M_w = 7.2$, 12 November 1999, Düzce, Turkey Earthquake, *Geophys. Res. Lett.* **28,** 367–370.

Ayhan, M. A., C. Demir, A. Kiliçoglu, *et al*. (1999). Crustal motion around the western segment of the north Anatolian fault zone: geodetic measurements and geophysical interpretation, *International Union of Geodesy and Geophysics (IUGG99),* 18–30 July, Birmingham, United Kingdom.

Barka, A. (1996). Slip distribution along the North Anatolian fault associated with the large earthquakes of the period 1939 to 1967, *Bull. Seism. Soc. Am.* **86,** 1238–1254.

Bürgmann, R., P. A. Rosen, and E. J. Fielding (2000). Synthetic aperture radar interferometry to measure Earth's surface topography and its deformation, *Annu. Rev. Earth Planet. Sci.* **28,** 169–209.

Bürgmann, R., P. Segall, M. Lisowski, *et al.* (1997). Postseismic strain following the 1989 Loma Prieta earthquake from GPS and leveling measurements, *J. Geophys. Res.* **102,** 4933–4955.

Du, Y., A. Aydin, and P. Segall (1992). Comparison of various inversion techniques as applied to the determination of a geophysical deformation model for the 1983 Borah Peak earthquake, *Bull. Seism. Soc. Am.* **82,** 1840–1866.

Ergintav, S., R. Bürgmann, S. McClusky, *et al*. (2002). Postseismic deformation near the İzmit earthquake (17 August 1999, *M* 7.5) rupture zone, *Bull. Seism. Soc. Am.* **92,** no. 1, 194–207.

Goldstein, R. M., and C. L. Werner (1998). Radar interferogram filtering for geophysical applications, *Geophys. Res. Lett.* **25,** 4035–4038.

Harris, R. A. (1998). Introduction to special section: stress triggers, stress shadows, and implications for seismic hazard, *J. Geophys. Res.* **103,** 24,347–24,358.

Harris, R., and P. Segall (1987). Detection of a locked zone at depth on the Parkfield, California segment of the San Andreas fault, *J. Geophys. Res.* **92,** 7945–7962.

Hearn, E. H., R. Bürgmann, and R. Reilinger (2002). Dynamics of İzmit earthquake postseismic deformation and loading of the Düzce earthquake hypocenter, *Bull. Seism. Soc. Am.* **92,** no. 1, 172–193.

Hubert-Ferrari, A., A. Barka, E. Jacques, *et al.* (2000). Seismic hazard in the Marmara Sea region following the 17 August 1999 İzmit earthquake, *Nature* **404,** 269–272.

Hudnut, K. W., L. Seeber, and J. Pacheco (1989). Cross-fault triggering in the November 1987 Superstition Hills earthquake sequence, southern California, *Geophys. Res. Lett.* **16,** 199–202.

Massonnet, D., and K. L. Feigl (1998). Radar interferometry and its application to changes in the earth's surface, *Rev. Geophys.* **36,** 441–500.

McClusky, S., S. Balassanian, A. Barka, *et al.* (2000). Global Positioning System constraints on plate kinematics and dynamics in the eastern Mediterranean and Caucusus, *J. Geophys. Res.* **105,** 5695–5720.

Meade, B., B. Hager, and R. Reilinger (2002). Estimates of seismic potential in the Marmara region from block models of secular deformation constrained by GPS measurements, *Bull. Seism. Soc. Am.* **92,** no. 1, 208–215.

Okada, Y. (1985). Surface deformation due to shear and tensile faults in a half-space, *Bull. Seism. Soc. Am.* **75,** 1135–1154.

Parsons, T., and D. S. Dreger (2000). Static-stress impact of the 1992 Landers earthquake sequence on nucleation and slip at the site of the 1999 $M = 7.1$ Hector Mine earthquake, southern California, *Geophys. Res. Lett.* **27,** 1949–1952.

Parsons, T., S. Toda, R. S. Stein, *et al.* (2000). Heightened odds of large earthquakes near Istanbul: an interaction-based probability calculation, *Science* **288,** 661–665.

Perfettini, H., R. S. Stein, R. Simpson, *et al.* (1999). Stress transfer by the 1988–1989 $M = 5.3$ and 5.4 Lake Elsman foreshocks to the Loma Prieta fault: unclamping at the site of peak mainshock slip, *J. Geophys. Res.* **104,** 20,169–20,182.

Reilinger, R. E., S. Ergintav, R. Bürgmann, *et al.* (2000). Coseismic and postseismic fault slip for the 17 August 1999, $M = 7.5$, İzmit, Turkey earthquake, *Science* **289,** 1519–1524.

Rosen, P. A., S. Hensley, H. A. Zebker, *et al.* (1996). Surface deformation and coherence measurements of Kilauea Volcano, Hawaii, from SIR-C radar interferometry, *J. Geophys. Res.* **101,** 23,109–23,125.

Savage, J. C. (1998). Displacement field for an edge dislocation in a layered half-space, *J. Geophys. Res.* **103,** 2439–2446.

Scharoo, R., and P. N. A. M. Visser (1998). Precise orbit determination and gravity field improvement for the ERS satellites, *J. Geophys. Res.* **103,** 8113–8127.

Sengör, A. M. C., N. Görür, and F. Saroglu (1985). Strike-slip faulting and related basin formation in zones of tectonic escape: Turkey as a case study, in *Strike-slip Faulting and Basin Formation,* K. T. Biddle and N. Christie-Blick (Editors), Soc. Econ. Paleont. Min. Spec. Publ., 227–264.

Stein, R. S., A. A. Barka, and J. H. Dietrich (1997). Progressive failure on the North Anatolian fault since 1939 by earthquake stress triggering, *Geophys. J. Int.* **128,** 594–604.

Straub, C., H.-G. Kahle, and C. Schindler (1997). GPS and geologic estimates of the tectonic activity in the Marmara Sea region, NW Anatolia, *J. Geophys. Res.* **102,** 27,587–27,601.

Toksöz, M. N., A. F. Shakal, and A. J. Michael (1979). Space-time migration of earthquakes along the North Anatolian fault zone and seismic gaps, *Pageoph* **117,** 1258–1270.

Wells, D. L., and K. J. Coppersmith (1994). New empirical relationships among magnitude, rupture length, rupture width, rupture area, and surface displacement, *Bull. Seism. Soc. Am.* **84,** 974–1002.

Wright, T. J., B. E. Parsons, and E. J. Fielding (2001). Measurement of interseismic strain accumulation across the North Anatolian fault by satellite radar interferometry, *Geophys. Res. Lett.* **28** (in press).

Wright, T. J., B. E. Parsons, J. Jackson, *et al.* (1999). Source parameters of the 1 October 1995 Dinar (Turkey) earthquake from SAR interferometry and seismic bodywave modelling, *Earth Planet. Sci. Lett.* **172,** 23–37.

Yagi, Y., and M. Kikuchi (1999). *http://wwweic.eri.u-tokyo.ac.jp/yuji/trk2/Turkeyafter.html.*

Department of Earth and Planetary Science and Berkeley Seismological Laboratory
301 McCone Hall
University of California–Berkeley
Berkeley, California 94720
burgmann@seismo.berkeley.edu
(R.B.)

Department of Geodesy
General Command of Mapping
Ankara, Turkey
(M.E.A., B.A., C.D., O.L., A.T.)

Mail Stop 300-233
Jet Propulsion Laboratory
California Institute of Technology
4800 Oak Grove Drive
Pasadena, California 91109
(E.J.F.)

Earth Resource Laboratory
Department of Earth Atmospheric, and Planetary Sciences
Massachusetts Institute of Technology
(S.M.)

Department of Earth Sciences
University of Oxford
Parks Road, Oxford
England, U.K.
(T.J.W.)

Manuscript received 22 September 2000.